Chapter 6

Field data examples

This chapter describes an application of the velocity estimation method and the angle-dependent reflector recovery method developed in this thesis for a field data set. I first describe the data set and its preprocessing. I then show the result of interval velocity model and angle-dependent reflectivity obtained by the method developed in this thesis.

6.1 Data description and preprocessing

The Mobil AVO data set includes seismic data and both petrophysical and well-log information from two wells that intersect with the seismic line. The seismic data consist of 1012 shot gathers recorded with an air gun source array with a shot interval of 25 meters. Each shot gather contains 120 traces with a receiver spacing of 25 meters.

The original data were significantly contaminated with free-surface and water-bottom multiples that makes identification of the primary reflections difficult. Lumley et al. (1995) preprocessed the data set so that it can be used for amplitude-preserved data processing. They applied a source and receiver consistent amplitude balancing to the seismic data and a time-domain conjugate-gradient multiple suppression technique to remove multiple reflection energy. Figure 6.1 shows a near-offset section and Figure 6.2 shows three CMP gathers that were corrected for time-varying spherical divergence (Newman, 1973), in addition to the preprocessing by Lumley et al. (1995).

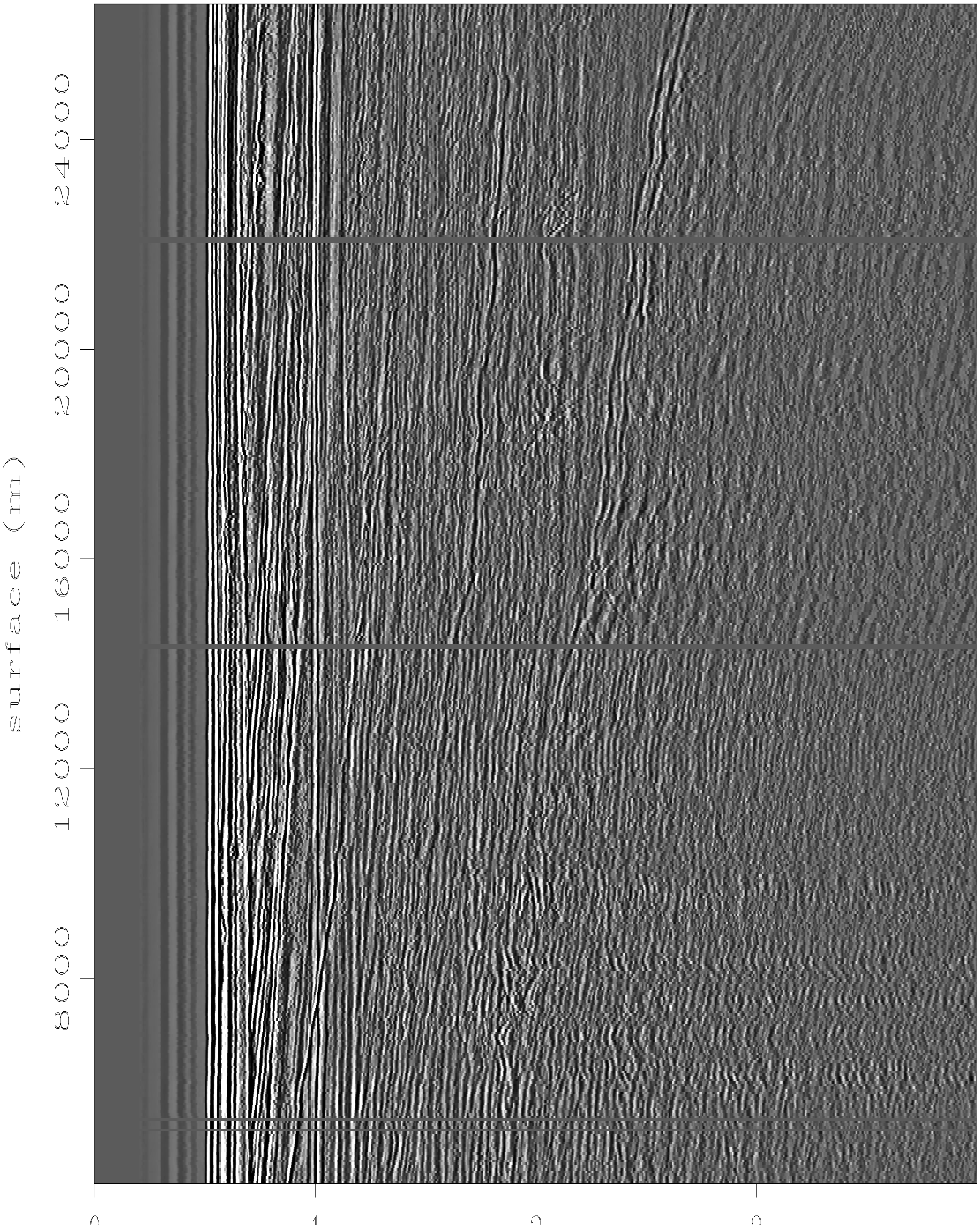

FIG. 6.1. Near-offset section of Mobil AVO dataset. examp-mo-near [NR]

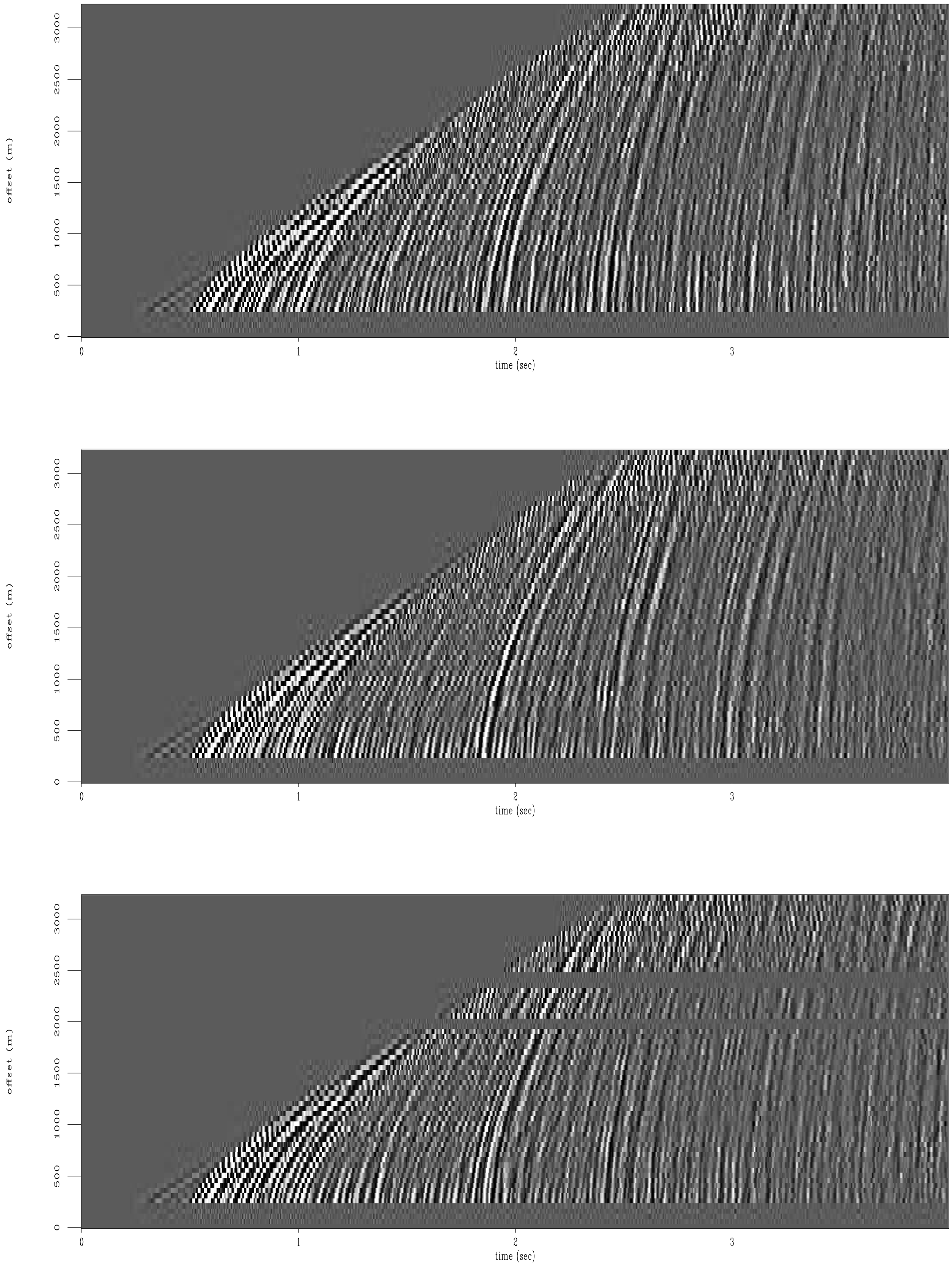

FIG. 6.2. CMP gathers section of Mobil AVO dataset. examp-mo-cmp [NR]

6.2 Near-offset trace interpolation

Mobil data set contains missing near-offset traces as well as a few randomly located missing traces, as shown in Figures 6.1 and 6.2. Those missing traces are interpolated by means of the iteratively-reweighted least-squares method that is explained in chapter 3. For each CMP gather, twenty iterations are performed in the conjugate-gradient algorithm. The result of interpolation is shown in Figure 6.3. It shows that both near-offset and randomly located missing traces were successfully interpolated and the interpolated traces follow the hyperbolic trend correctly in CMP gathers.

6.3 Tomographic velocity estimation

In order to perform the tomographic velocity estimation, the first step is to pick reflectors in the image domain after migration with a velocity model that is first guess. Figure 6.4 shows the initial velocity model that was used. The initial velocity model was determined by setting $1500(m/s)$ for the water velocity and linearly increased with respect to depth from the ocean bottom. Figure 6.5 shows the image obtained by stacking thirty-one images of the surface-oriented plane-wave synthesis imaging with -30 through $+30$ degrees for the incidence angle range. Figure 6.6 shows some of the CSL gathers selected from the image cube before stack and reveals velocity error by showing curvatures of the reflector images from horizontal aligning with respect to the incidence angles. I manually picked eight reflectors to be used for velocity analysis; these are displayed in Figure 6.7.

The next step in the tomographic velocity estimation process is the measurement of traveltime errors along the reflector picked. In the algorithm proposed in this thesis (chapter 4), the traveltime errors are inferred from the residual moveout (RMO) velocity measured. The RMO velocity analysis is performed along the reflector picked and the results of it are shown in Figure 6.8.

Finally the traveltime errors are back projected to obtain the slowness field error of the reference model. This requires the calculation of the back projection operator by means of ray tracing. A modified reflector location using the RMO velocity is used to trace rays instead of using the reflector picked as the starting location of the ray tracing, The modified reflector locations are shown in Figure 6.9. Figure 6.10 shows the updated velocity model that is obtained by inversion of the traveltime errors.

The prestack data set is again imaged with the updated velocity model by means of plane wave synthesis imaging; the new image is shown in Figure 6.11. The CSL gathers shown in Figure 6.12 confirm the accuracy of the velocity updated by showing horizontal alignment of the images with respect to the incidence angle.

6.4 Angle-dependent reflectivity recovery

Thirty-one plane waves are synthesized with incidence angles that varys from -30 degrees to $+30$ degrees, in order to retrieve the angle-dependent reflectivity. For obtaining common incidence angle image section, I chose twenty-one depth levels for datum planes to synthesize the plane-wave with the corresponding incidence angle, and I extracted and patched the portions of the image near the datum planes to produce the common incidence angle image section.

In order to show the global AVO trend of the subsurface, a hydrocarbon indicator (HCI) section (Lumley et al., 1995) was computed using near and far incidence angle reflectivity amplitudes. The angle-dependent reflectivity images were partially stacked into two reflection-angle ranges: 0-15 degrees, and 15-30. Call these two parameter sections "near" N and "far" F. A reasonable HCI section (Figure 6.13) was then obtained using the composite indicator:

$$HCI = N(N - F) \tag{6.1}$$

This N,F technique does not contain as much AVO information as impedance contrast sections, but has a higher S/N ratio.

6.5 Summary

In this chapter I have shown an example of the sequential inversion approach developed in this thesis using a field data set. For the field data, I used Mobil's AVO dataset, which was preprocessed by Lumley et al.(1995). The interpolation scheme produced events that reasonably follow the rest of the known hyperbolic event in the CMP gather. The tomographic velocity estimation method succeeded in reducing residual moveout in the migrated images. The final HCI section obtained by the angle-dependent reflectivity imaging displayed a strong anomaly at the known top reservoir location.

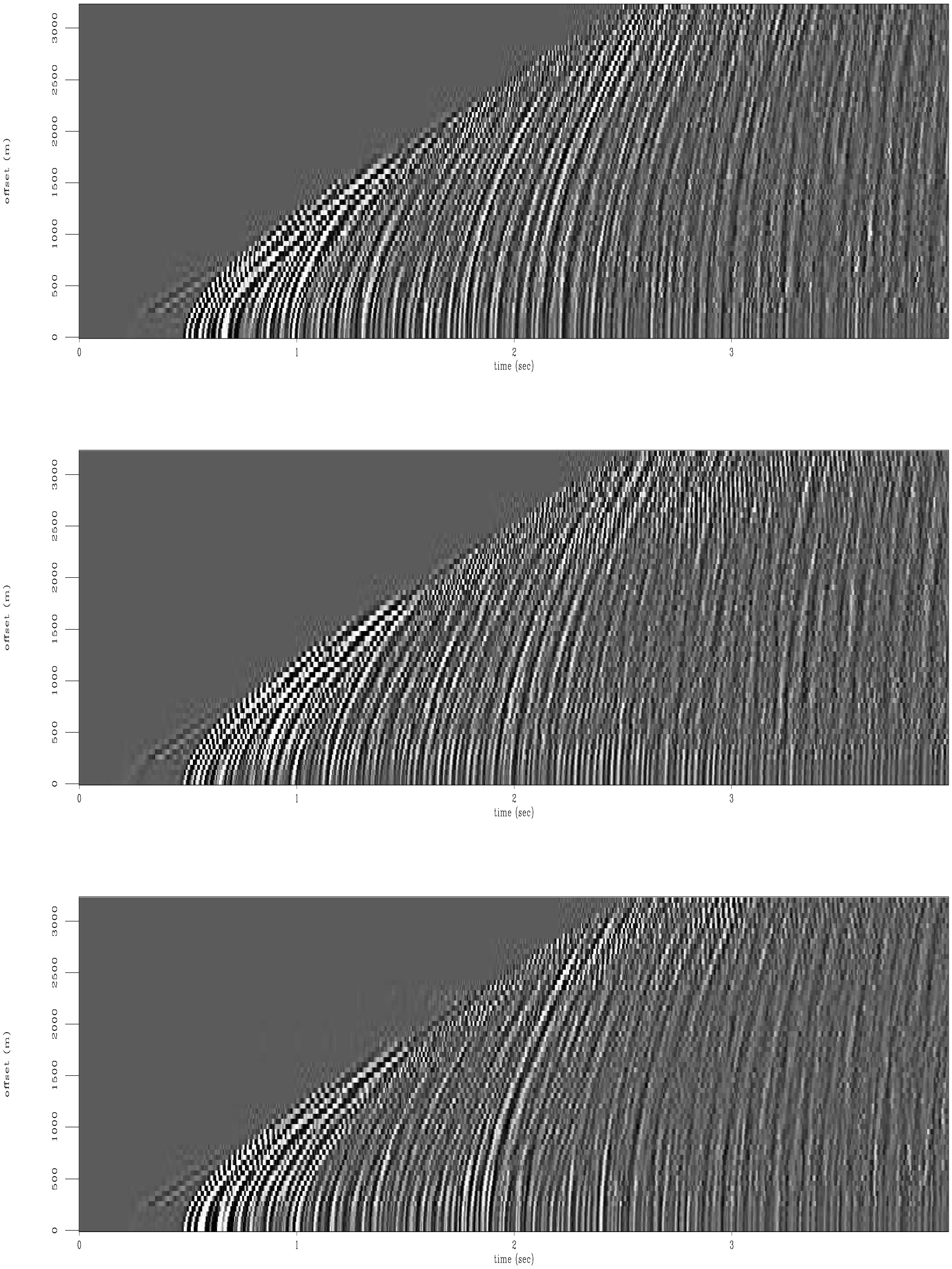

FIG. 6.3. CMP gathers section of Mobil AVO dataset after interpolation. examp-moint-cmp [CR]

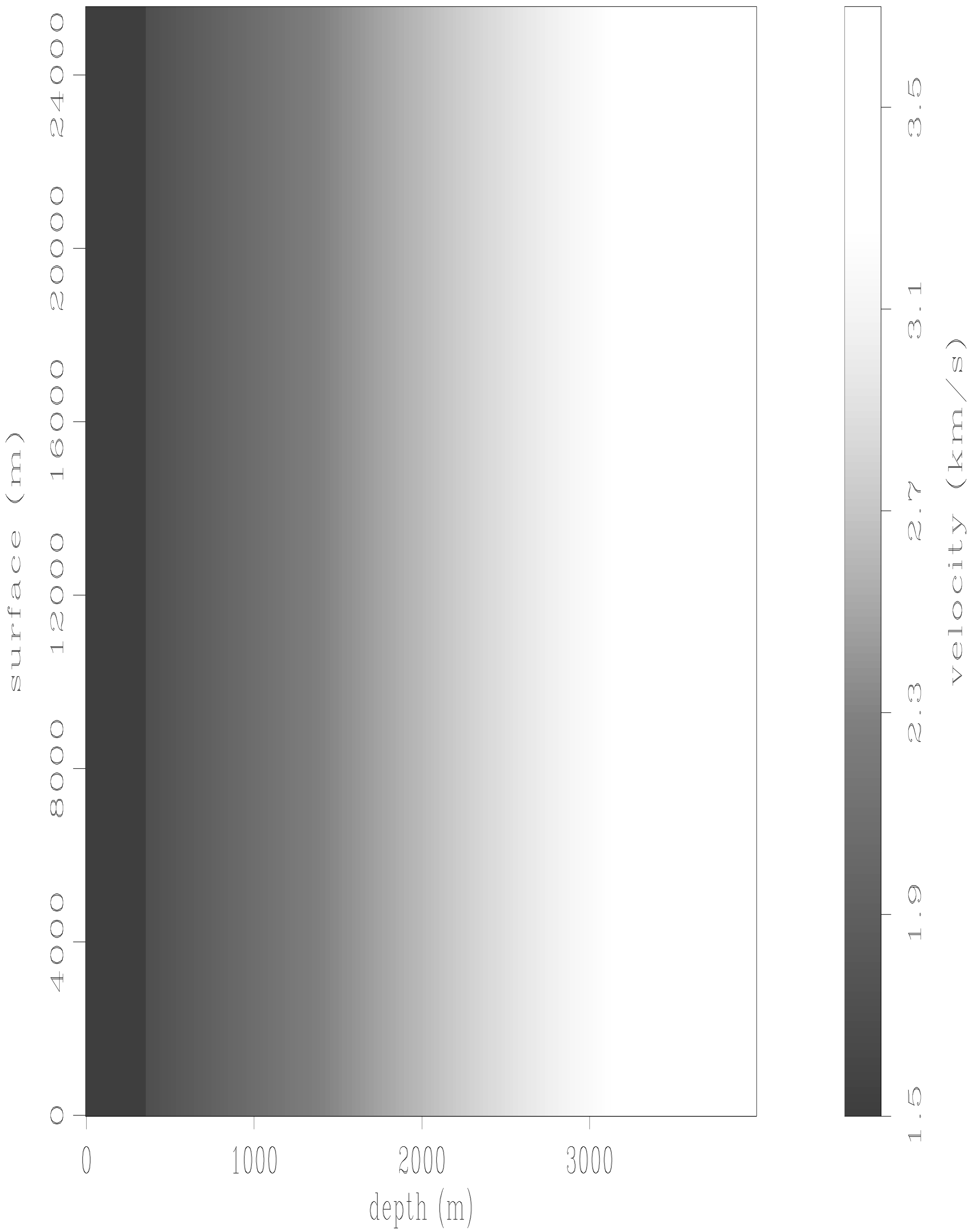

FIG. 6.4. Velocity model of initial guess. examp-mo-vel-iter0 [R]

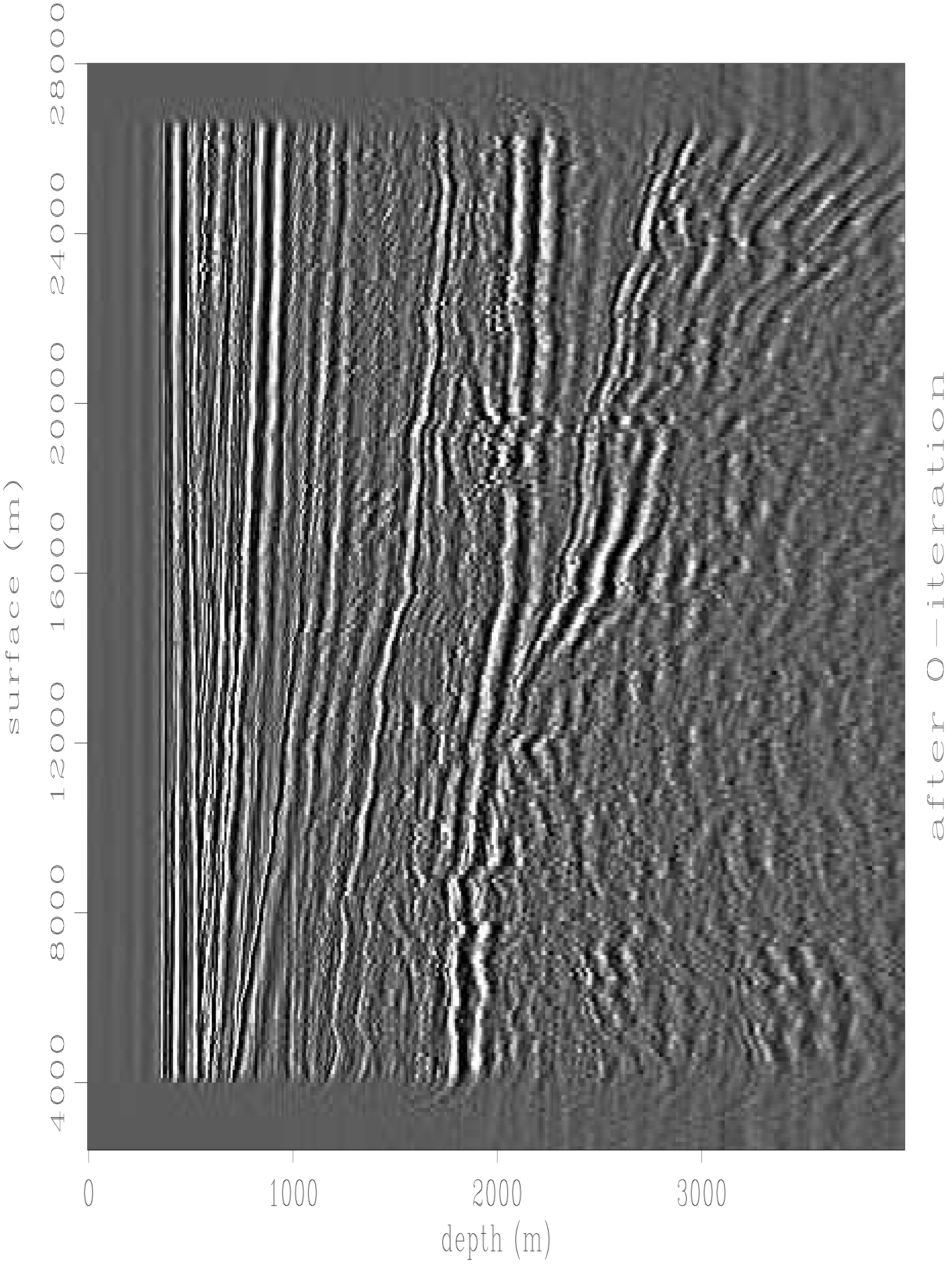

FIG. 6.5. Image obtained by thirty-one plane wave syntheses. examp-pws-mo-iter0 [NR]

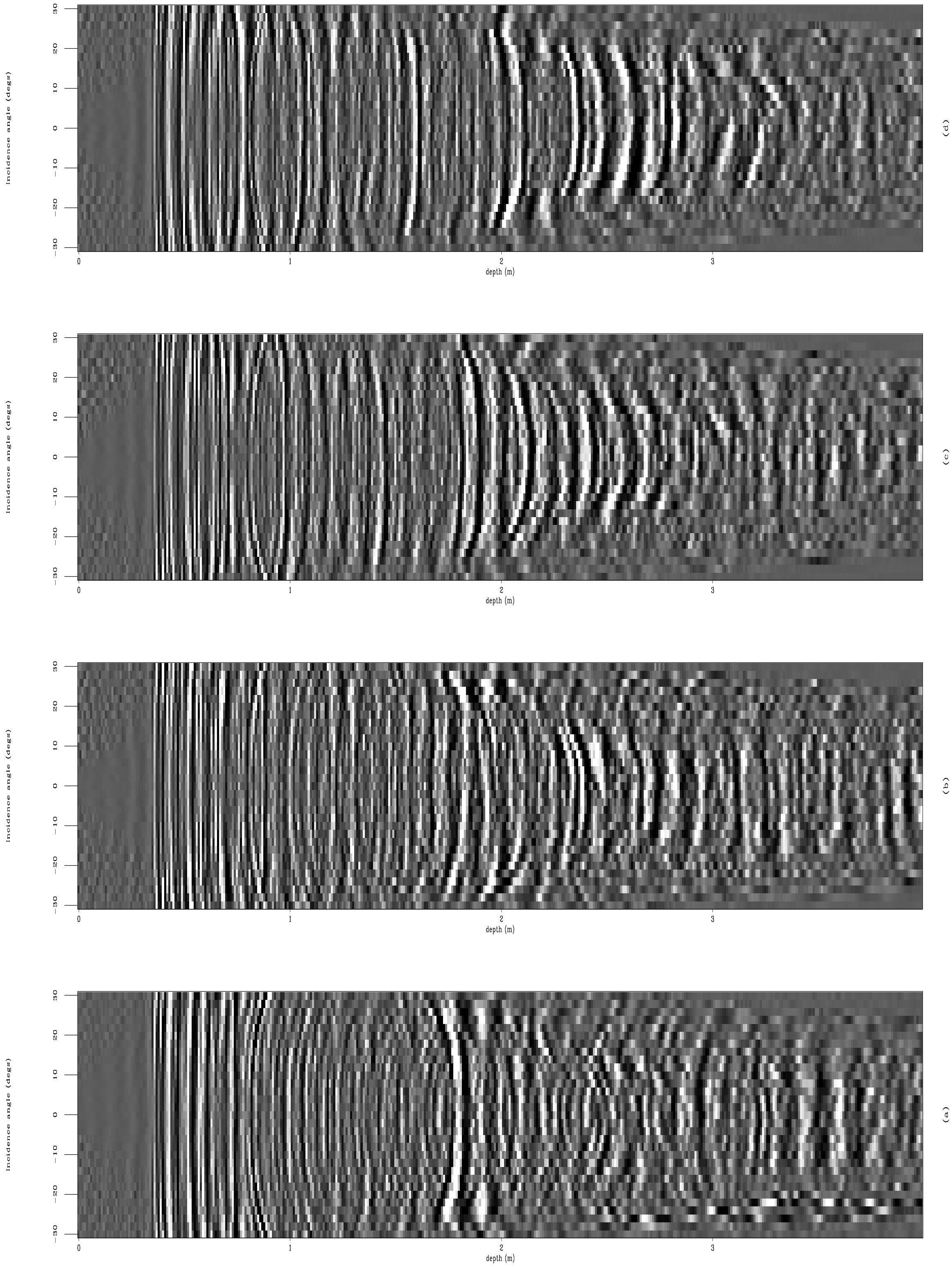

FIG. 6.6. Selected CSL gathers after zero-iterations. $\boxed{\text{examp-crps-iter0}}$ [NR]

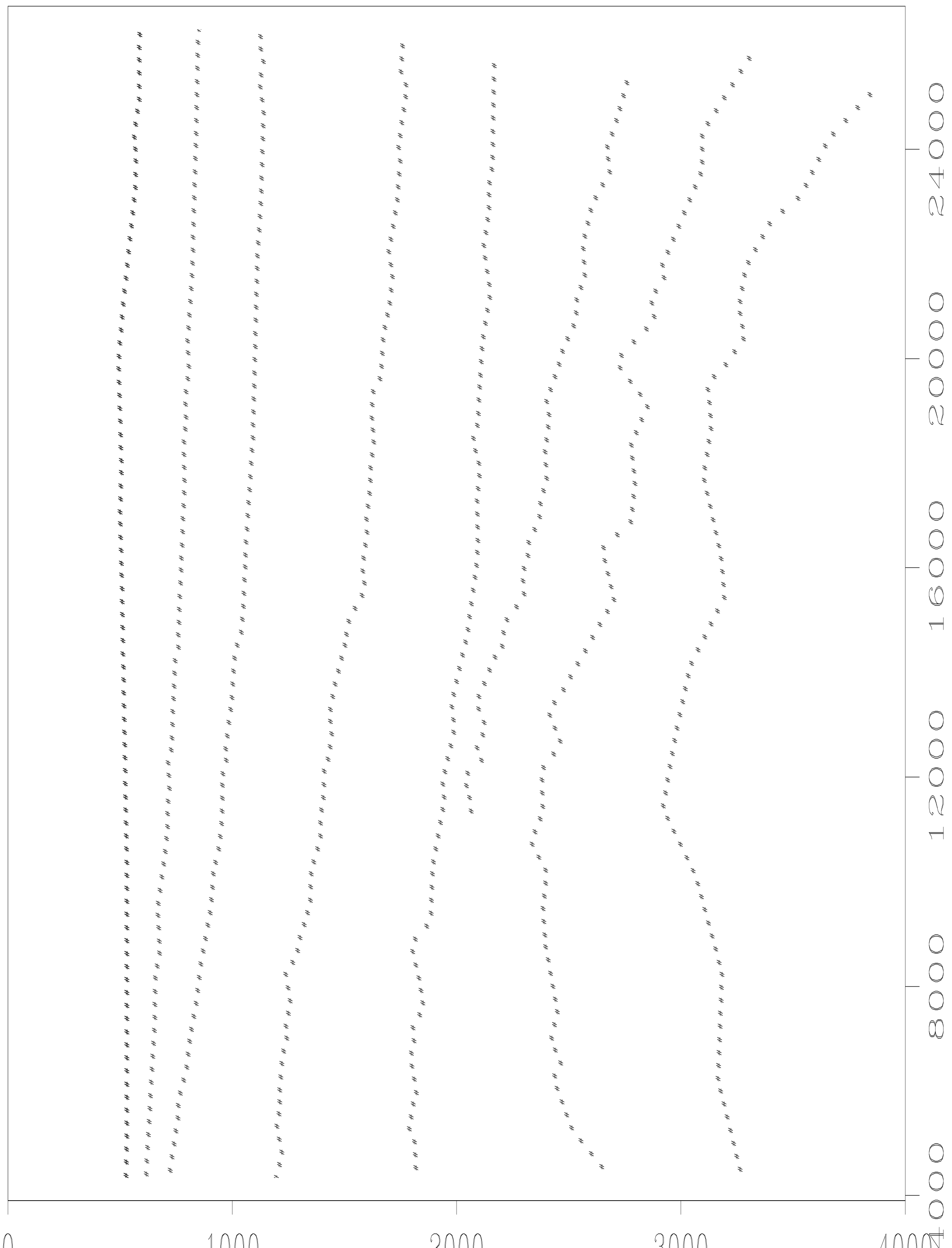

FIG. 6.7. Reflector locations picked for tomographic inversion. examp-pick-mo-iter0 [NR]

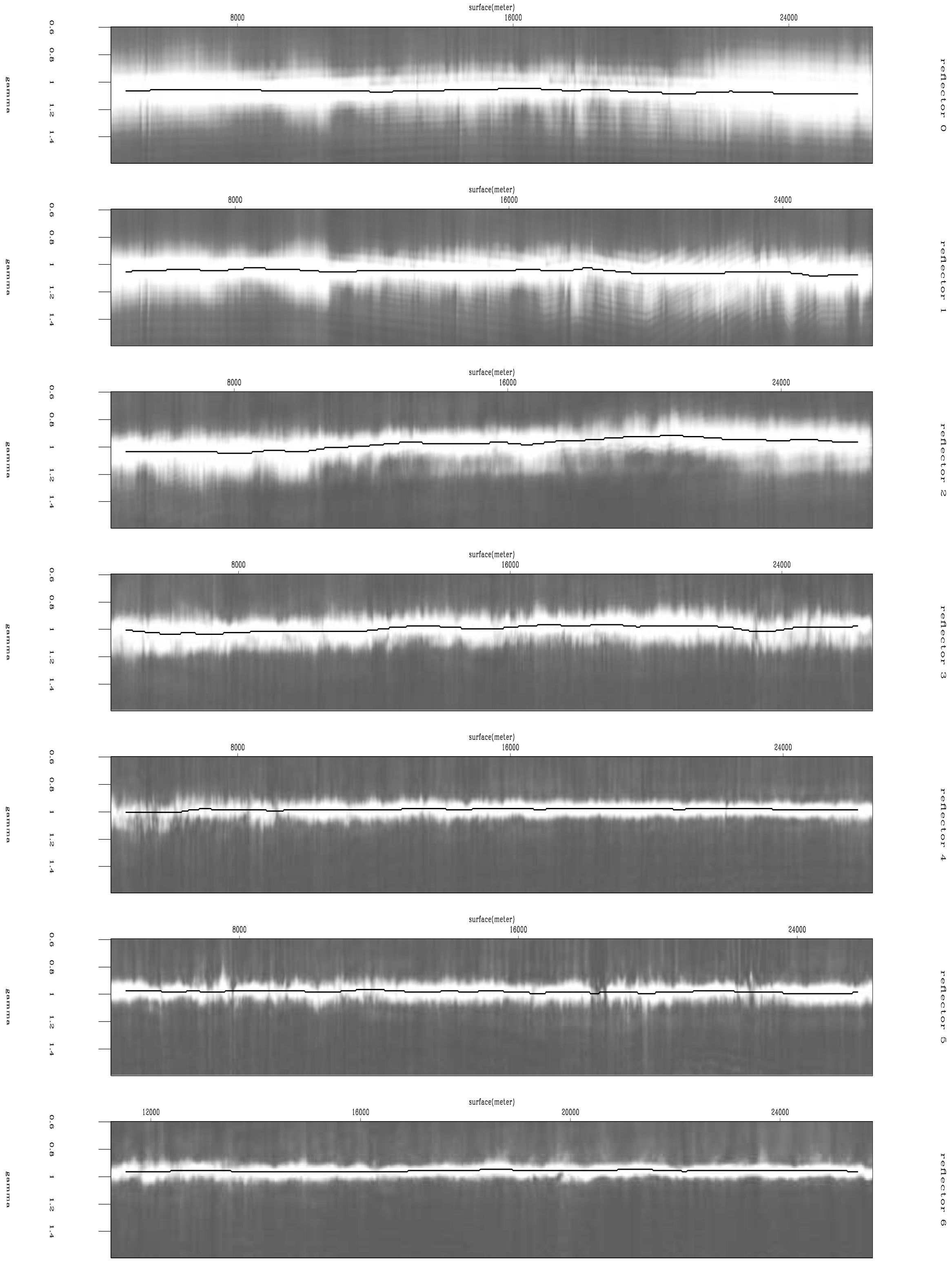

FIG. 6.8. Reflector locations positioned according to RMO velocity. examp-velan-iter0 [NR]

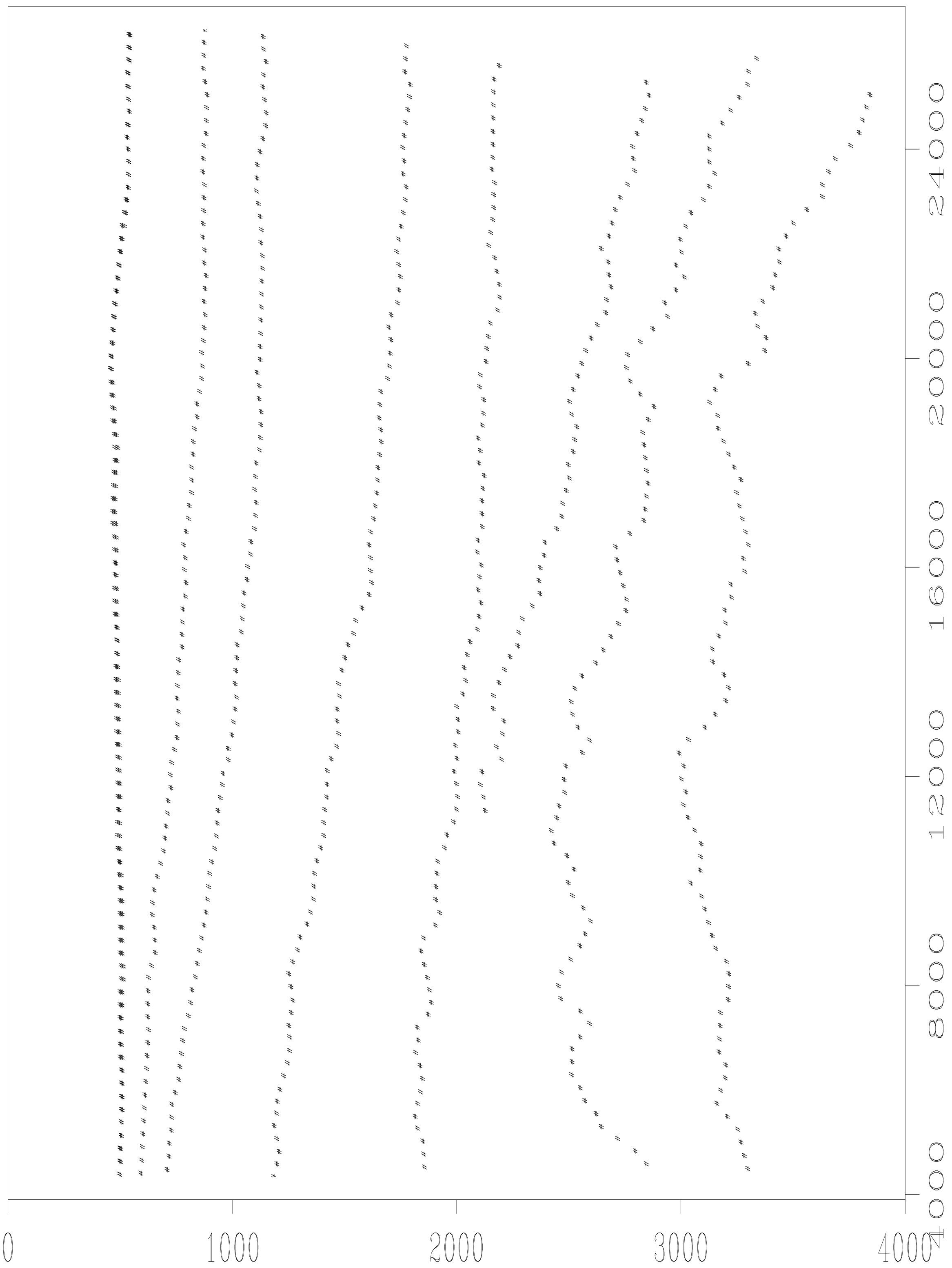

FIG. 6.9. Reflector locations positioned according to RMO velocity. examp-rfloc-mo-iter0 [NR]

FIG. 6.10. Velocity model after one iteration of tomographic velocity estimation. examp-mo-vel-iter1 [NR]

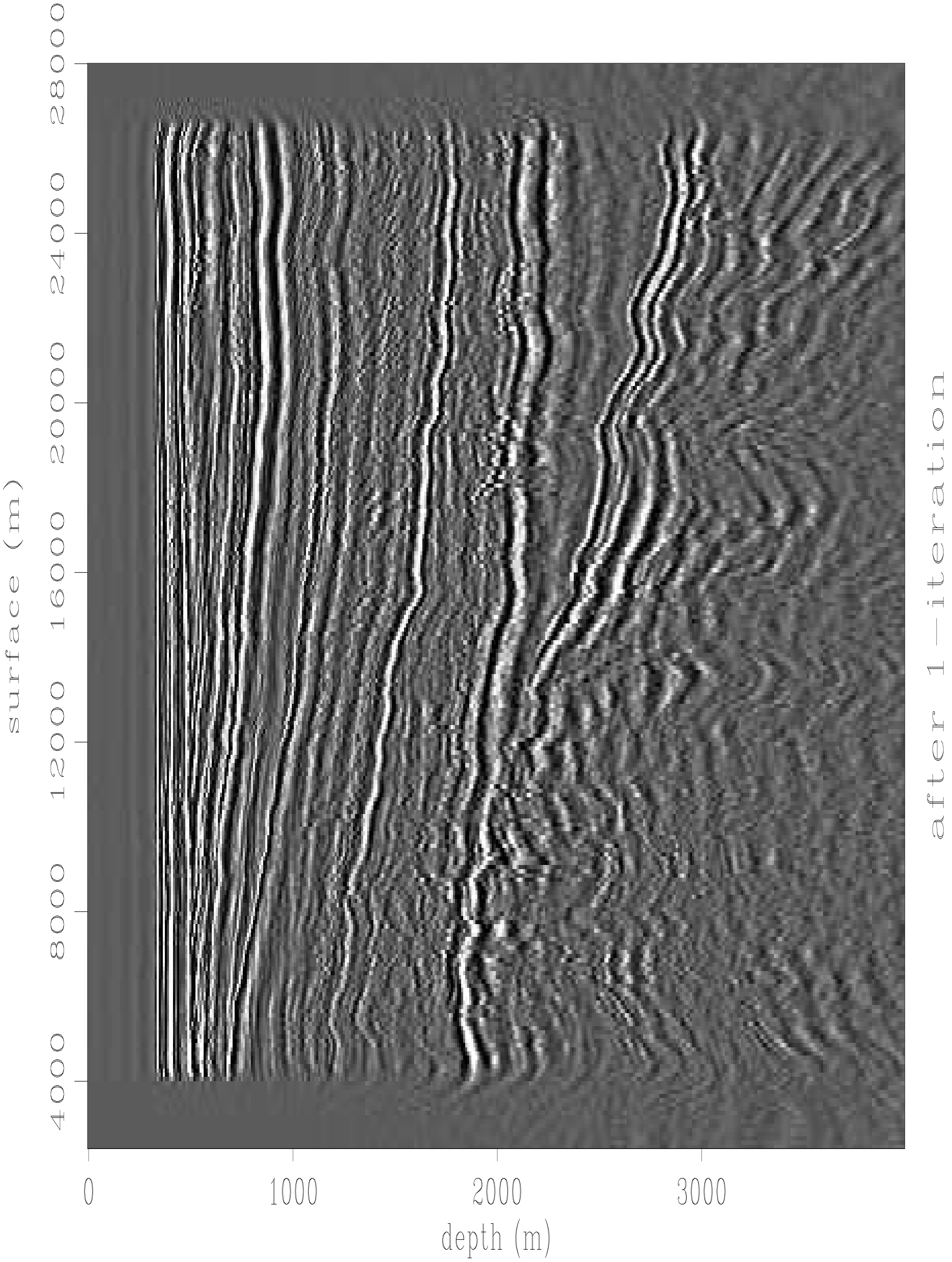

FIG. 6.11. Image obtained by thirty-one plane wave syntheses. examp-pws-mo-iter1 [NR]

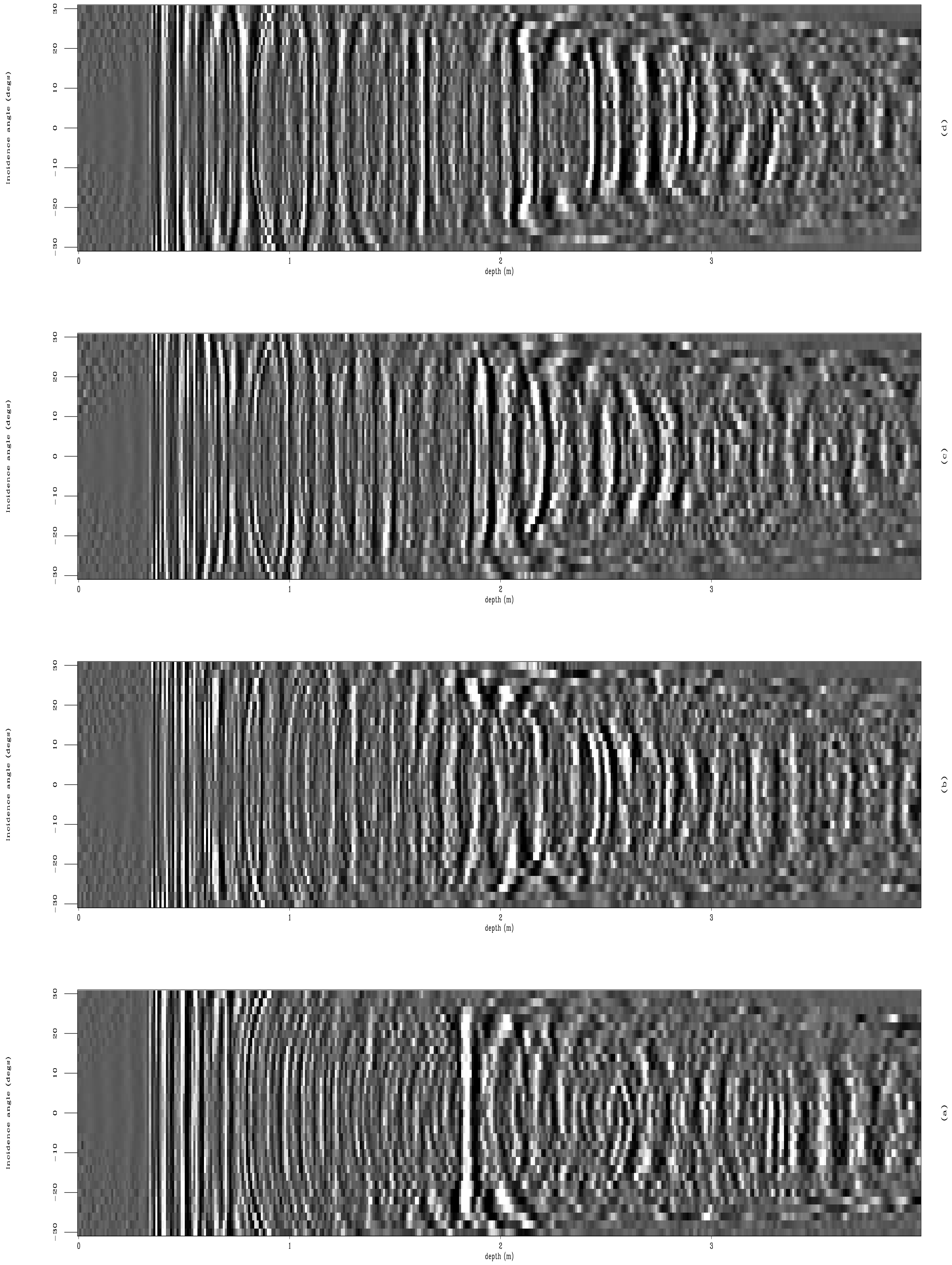

FIG. 6.12. Selected CSL gathers after one-iteration. examp-crps-iter1 [NR]

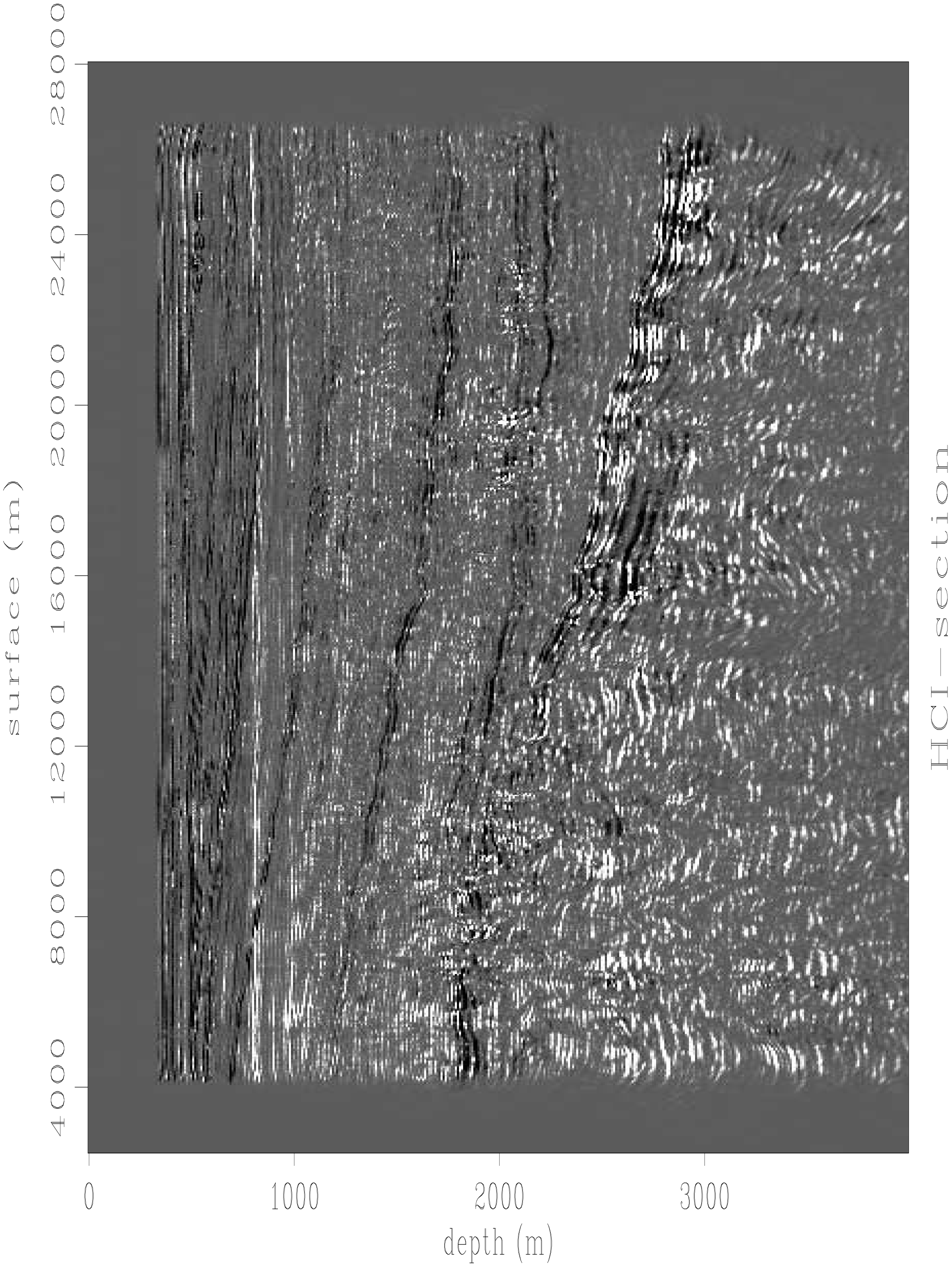

FIG. 6.13. Hydrocarbon indicator (HCI) section. examp-hci [NR]